

Light Conversion Control in NIR-Emissive Optical Materials Based on Heterolanthanide Er_xYb_{3-x} Quinolinolato Molecular Components

Flavia Artizzu,^{*,†,‡} Francesco Quochi,^{*,‡} Luciano Marchiò,[§] Cristiana Figus,[‡] Danilo Loche,[†] Matteo Atzori,[†] Valerio Sarritzu,[‡] Anna M. Kaczmarek,[⊥] Rik Van Deun,[⊥] Michele Saba,[‡] Angela Serpe,[†] Andrea Mura,[‡] Maria Laura Mercuri,[†] Giovanni Bongiovanni,[‡] and Paola Deplano^{*,‡}

[†]Dipartimento di Scienze Chimiche e Geologiche and [‡]Dipartimento di Fisica, University of Cagliari, SS 554 Bivio per Sestu, I-09042 Monserrato, Cagliari, Italy

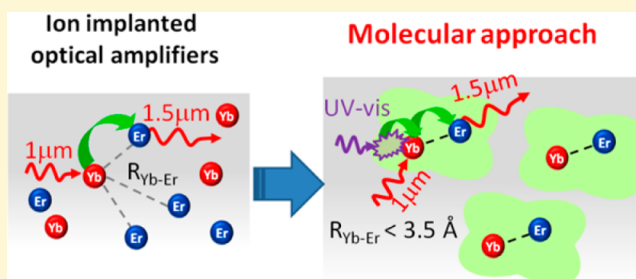
[§]Dipartimento di Chimica, University of Parma, Parco Area delle Scienze 17/A, I-43100 Parma, Italy

[⊥]L3- Luminescent Lanthanide Lab, f-Element Coordination Chemistry, Department of Inorganic and Physical Chemistry, Ghent University, Krijgslaan 281-S3, B-9000 Ghent, Belgium

S Supporting Information

ABSTRACT: Homo- and heterobimetallic homoleptic complexes of general formula Er_xYb_{3-x}Q₈ (Q = 8-quinolinolato; $x = 0, 1, 2, 3$) and the corresponding heteroleptic complexes Er_xYb_{3-x}Q₈NO₃ ($x = 0, 1b; x = 1, 2b; x = 2, 3b$), where one Q ligand is replaced by a nitrate anion, have been synthesized and fully characterized by means of compositional (energy-dispersive X-ray spectrometry, inductively-coupled plasma-mass spectrometry, and electrospray ionization mass spectrometry) and structural (X-ray diffraction) investigations to study the effects of ligand substitution and variation of metal composition on their chemical and photophysical properties.

Advanced spectroscopic and photophysical studies in the visible and near-infrared spectral regions have allowed the achievement of a detailed picture of the photocycle leading to narrow-band lanthanide luminescent emission, providing evidence of highly efficient ligand-to-metal and metal-to-metal (Yb-to-Er) resonance energy transfers thanks to the short intermetallic distances in heterolanthanide molecular species. Highly homogeneous silica thin films doped with **2** have shown to retain the optical properties of the dopant complex in solution, proving the suitability of this class of complexes for preparing Er/Yb codoped optical materials for potential applications as waveguides or amplifiers with controlled composition and distribution of the optically active metals.



INTRODUCTION

Near-infrared (NIR) emitting lanthanide (Ln) ions are of remarkable interest in view of the several potential applications ranging from optical technologies to biomedical fields.^{1,2} Among them, Yb³⁺ and Er³⁺ play a special role in telecom technologies, as their emission can be exploited for signal amplification in the so-called first- and third-communication windows, at 1 and 1.5 μm wavelengths, respectively. Doped silica fibers such as EDFAs (erbium-doped fiber amplifiers) are currently used for optical amplification in the long-haul communication systems operating in the 1.5 μm spectral window. However, for effective optical pumping of intrinsically weakly absorbing lanthanide ions, highly efficient light-harvesting “antennas” are required for resonance energy transfer (RET) to the higher energy levels of these metal emitters. Er³⁺ sensitization through RET from Yb³⁺, featuring a 10-times higher absorption cross-section, has proved to be a smart strategy to achieve enhancement of Er³⁺ emission at 1.5 μm in Yb–Er codoped glassy optical fiber amplifiers.^{3–8} For efficient Yb-to-Er RET through the distance-dependent, through-space

Förster’s mechanism, the two optically active ions must lie at close distance (<10 Å).⁹ Most of the codoped Er/Yb materials so far studied in view of their potential applications, especially as NIR optical waveguides and amplifiers, consist of inorganic glassy or polymeric matrices where the two optically active ions are incorporated through diverse techniques such as ion implantation, sputtering, electron beam lithography, melting techniques, or via the sol–gel process to cite the most popular.^{3–8} However, controlled codoping of inorganic or polymeric matrices with lanthanide inorganic salts or oxides is usually limited by solubility reasons or intrinsic difficulties in regulating the distribution and relative positions of the two intercommunicating ions into the host matrix. A viable route to address this challenging task relies on the use of easily processable discrete polynuclear molecules where selected lanthanide ions are held together in fixed positions in a

Received: March 25, 2015

Revised: May 6, 2015

pre-designed molecular architecture allowing controlled inter-metallic RET between two closely spaced optically active ions. The incorporation of the lanthanide ions into an organic framework can help to overcome solubility restraints in inorganic/organic hosts while improving the thermal stability and mechanical strength of coordination complexes compared to conventional inorganic or polymeric materials. Moreover, in these heterometallic assemblies, suitable organic ligands can be introduced as efficient “light harvesters”, providing a supplementary excitation channel for the lanthanide ions. In this way, it would be possible to take advantage of the molecular approach for functional heterolanthanide assemblies while fabricating optical materials useful for direct applications.

Recently, it has been demonstrated that the Ln_3Q_9 ($\text{Q} = 8$ -quinolinolato) framework is particularly suitable for preparing heteronuclear-lanthanide complexes,¹⁰ providing several benefits especially in regard to NIR-emitters: (i) high coordinating ability toward different Ln ions across the whole series;^{11–15} (ii) excellent antenna properties of the Q ligand allowing simultaneous excitation of different NIR-emissive Ln ions upon single-wavelength irradiation in the easily accessible visible region;^{16,17} (iii) short intermetallic distances (below 3.5 Å), optimal for ensuring fully efficient Yb-to-Er RET;^{9–15} and (iv) high stability and capability to undergo processing procedures (in solution or by vacuum deposition) without alterations.^{18–25}

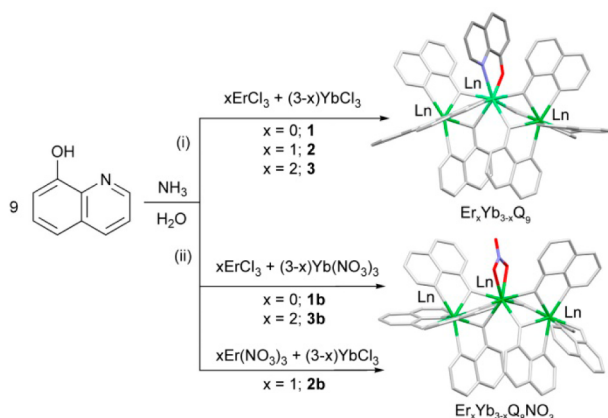
To further explore and clarify the chemical/photophysical properties of mixed Er/Yb quinolinolates, a thorough study on the structure/properties relationship upon slight structural modifications (replacement of one Q ligand) and variation of metal composition has been performed, and results have been compared to those observed for the corresponding trinuclear homometallic Yb quinolinolato analogs as useful references. In addition, the potential of this class of compounds as functional molecular materials for photonic applications has been investigated through the incorporation of these complexes into silica thin films.

RESULTS AND DISCUSSION

Synthesis, Structural, and Analytical Characterization.

The investigated compounds have been prepared through a one-pot reaction between the selected metal salts and the ligand in suitable ratios, taking advantage of the very similar reactivity of the erbium and ytterbium ions both belonging to the second half of the lanthanide series, according to the reaction pathways (i) and (ii) illustrated in Scheme 1.

Scheme 1. Reaction Pathways



Homoleptic $\text{Er}_x\text{Yb}_{3-x}\text{Q}_9$ complexes have been synthesized with the procedure already described for the Er_3Q_9 and mixed lanthanide (Yb, Er, Nd) complexes^{10,12} by directly reacting the deprotonated Q ligand with chloride (or acetate) salts of Yb and Er ions in selected molar ratios ($x = 0, 1, 2, 3$; reaction pathway (i), Scheme 1). $\text{Er}_x\text{Yb}_{3-x}\text{Q}_9$ formulations are in agreement with analytical and spectroscopic data (see Experimental Section). The molecular structure of **2** has been recently reported elsewhere,¹⁰ and the isostructurality of compounds **1** and **3** with respect to **2** was confirmed by powder X-ray diffraction (XRD) measurements performed on microcrystalline samples obtained after recrystallization in CH_3CN (Figure S1, Supporting Information).

Instead, when using, as metal source, salts of the more coordinating nitrate anion in the presence of two equivalents of the chloride salt of a second lanthanide ion, heteroleptic complexes of general formula $\text{Er}_x\text{Yb}_{3-x}\text{Q}_8\text{NO}_3$ have been isolated ($x = 0, \mathbf{1b}; x = 1, \mathbf{2b}; x = 2, \mathbf{3b}$; reaction pathway (ii), Scheme 1), as confirmed by analytical and spectroscopic data (see Experimental Section). Single crystals suitable for X-ray structural analysis have been obtained for **1b** after recrystallization in CH_3CN . The molecular structure of **1b** is shown in Figure 1.

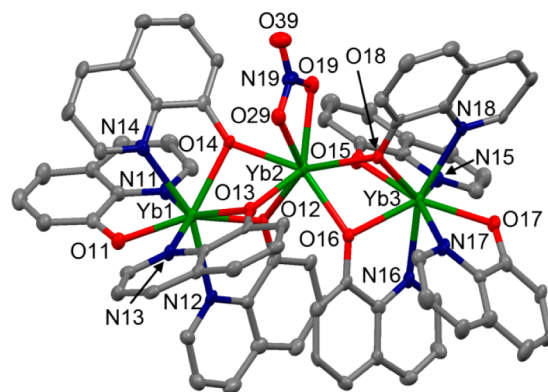


Figure 1. Molecular structure of **1b** with H atoms omitted for clarity.

The molecule, which can be formulated as $\text{Yb}_3\text{Q}_8\text{NO}_3$, presents a trinuclear structural arrangement similar to the analogous homoleptic Ln_3Q_9 complexes,^{12–15} with a nitrate anion replacing one quinolinolato ligand chelating the central Yb^{3+} ion. The three coordination sites are inequivalent, and the two outer metals are in a N_4O_4 environment through coordination of four quinolinolato ligands, whereas the inner metal is octa-coordinated by six oxygen atoms of bridging μ^2 -quinolinolato ligands and two oxygen atoms of a κ^2 - NO_3 anion. Interestingly, the $\text{Yb}(1)\text{--Yb}(2)\text{--Yb}(3)$ angle is 139.6° and is remarkably wider than in the analogous homoleptic Ln_3Q_9 complexes obtained with the synthetic method (i) in Scheme 1, Er_3Q_9 (133.5°),¹² ErYb_2Q_9 (133.4°), and NdErYbQ_9 (132.4°),¹⁰ and slightly smaller than that found for Yb_3Q_9 (140.3°).¹⁴ It is also worth noting that the $\text{Yb}(1)\cdots\text{Yb}(2)$ and $\text{Yb}(2)\cdots\text{Yb}(3)$ distances in **1b** are 3.414 Å and 3.407 Å and are noticeably shorter than those found in the homoleptic Yb_3Q_9 (3.459 and 3.458 Å)¹⁴ and also in the mixed ErYb_2Q_9 (**2**, 3.475 Å and 3.478 Å)¹⁰ complexes. Moreover, the difference in the metal separation lengths between Er_3Q_9 (3.488 and 3.495 Å)¹² and **1b** significantly exceeds the difference of erbium and ytterbium ionic radii ($\Delta r_{\text{Er--Yb}}^{\text{CN}=8} = 1.9$ pm). This may be likely ascribed to the lower steric hindrance of the nitrate anion

coordinated to the central metal with respect to the quinolinolato ligand, allowing the metal centers to sit at closer proximity in the trinuclear molecular framework. As far as the molecular crystal packing is concerned, the presence of the coordinated nitrate anion does not induce significant differences in terms of supramolecular interactions with the surrounding molecules with respect to those exchanged in their homoleptic analogues. The isostructurality of compounds **2b** and **3b** with respect to **1b** was confirmed by powder-XRD measurements on microcrystalline samples obtained after recrystallization in CH₃CN (Figure S1, Supporting Information). Main crystallographic parameters and most significant bond lengths for **1b** are reported in Tables 1 and 2, respectively.

Table 1. Summary of X-ray Crystallographic Data for 1b

empirical formula	C ₇₂ H ₄₇ N ₉ O ₁₁ Yb ₃
color, habit	yellow, block
cryst syst, space group	triclinic P-1
a, b, c (Å)	12.7218(8), 15.1809(10), 18.0938(11)
α, β, γ (deg.)	95.563(2), 103.475(2), 111.631(2)
V (Å ³)	3093.6(3)
Z, ρ(calc) (Mg/m ³)	2, 1.861
T (K), λ (Å)	125(2), 0.71073
μ (mm ⁻¹)	4.570
θ range (deg.)	2.36–25.03
no. of rflns/unique	40882/10916
GOF	1.002
final R indices [I > 2σ(I)]	R1 = 0.0524, wR2 = 0.1106

Table 2. Selected Bond Lengths for 1b

N(11)–Yb(1)	2.425(9)	O(16)–Yb(3)	2.315(6)
N(12)–Yb(1)	2.466(9)	O(17)–Yb(3)	2.237(7)
N(13)–Yb(1)	2.489(8)	O(18)–Yb(3)	2.325(7)
N(14)–Yb(1)	2.472(9)	O(12)–Yb(2)	2.347(7)
N(15)–Yb(3)	2.485(8)	O(13)–Yb(2)	2.251(6)
N(16)–Yb(3)	2.436(9)	O(14)–Yb(2)	2.305(7)
N(17)–Yb(3)	2.445(9)	O(15)–Yb(2)	2.240(7)
N(18)–Yb(3)	2.433(8)	O(16)–Yb(2)	2.269(7)
O(11)–Yb(1)	2.219(7)	O(18)–Yb(2)	2.395(7)
O(12)–Yb(1)	2.301(6)	O(19)–Yb(2)	2.382(7)
O(13)–Yb(1)	2.304(7)	O(29)–Yb(2)	2.393(7)
O(14)–Yb(1)	2.339(6)	Yb(2)–Yb(1)	3.4139(7)
O(15)–Yb(3)	2.295(7)	Yb(2)–Yb(3)	3.4071(7)

Inductively coupled plasma–mass spectrometry (ICP–mass) analysis on solution samples has been employed to accurately assess metal composition in mixed Er/Yb compounds, and the following stoichiometrical formulations have been retrieved: Er_{0.89}Yb_{2.11}Q₉ (**2**); Er_{1.92}Yb_{1.08}Q₉ (**3**); Er_{0.88}Yb_{2.12}Q₈NO₃ (**2b**); Er_{1.95}Yb_{1.05}Q₈NO₃ (**3b**). These results evidence a small excess (2–4%) of Yb content with respect to expected stoichiometrical metal ratios, Er/Yb 2:1 (**2**, **2b**) or 1:2 (**3**, **3b**) used in the synthetic procedures. Results are quite consistent, with only small variations, within the series of four independent samples, pointing out a slightly stronger affinity of Yb³⁺ upon coordination to the 8-quinolinolato ligand likely related to its slightly smaller ionic radius compared to Er³⁺.

Generally, when using one-pot synthetic approaches for the preparation of heterolanthanide compounds, in the absence of some metal selectivity restrictions, statistical metal distribution over the available coordination sites leading to mixtures of

homo- and heterolanthanide species is predictable.^{26,27} For this reason, to reach a detailed picture of molecular speciation of the mixed Er/Yb compounds and explore the reactivity of the different Ln ions upon ligand coordination, positive ion mode electrospray ionization (ESI)–mass experiments have been performed, and corresponding spectra for **2**, **2b**, **3**, and **3b** are reported in Figure 2. As expected, for all the samples, two peaks are dominant. The peak at highest *m/z* (1640–1680 *m/z*) corresponds to an isotopic distribution of [Er_xYb_{3-x}Q₈]⁺ (*x* = 0–3) species as a consequence of the fragmentation of one Q ligand for **2** and **3** (Figure 2a) and a nitrate anion for **2b** and **3b** (Figure 2b) from the parent molecule. The second peak at 1045–1075 *m/z* is related to [Er_xYb_{2-x}Q₅]⁺ (*x* = 0–2) fragments. It is worth noting that in the spectra of **2b** and **3b**, no peaks of significant intensity can be attributed to [Er_xYb_{3-x}Q₇NO₃]⁺ (*x* = 0–3) or [Er_xYb_{2-x}Q₄NO₃]⁺ (*x* = 0–2) fragments (see Supporting Information). This suggests that the chelating ligand at the central coordination site in the trinuclear complexes is the most weakly bound, in agreement with previous results supported by time-dependent density functional theory (TD-DFT) calculations on similar compounds.¹⁴ The isotopic distribution of the parent peak for all the mixed complexes reveals that the most predominant species is [ErYb₂Q₈]⁺ (*m/z* = 1666.2) for **2** and **2b** and [Er₂YbQ₈]⁺ (*m/z* = 1660.2) for **3** and **3b** and confirms that multiple species with different metal ratios are present in the samples. Experimental spectra are in fact in good agreement with models (dotted lines, Figure 2) calculated by taking into account the molecular speciation estimated for a statistical distribution of the metals across the three coordination sites, on the basis of ICP–mass metal compositional analysis. Relative abundances of homo- and heterometallic species constituting samples **2**, **3**, **2b**, and **3b** are reported in Table 3.

Given the close similarity of Er³⁺ and Yb³⁺ ionic radii, these results are not surprising, although it has been recently observed that a remarkable size discriminating effect controls molecular speciation in heterolanthanide quinolinolates when a larger ion, such as neodymium, is mixed with smaller lanthanides belonging to the second half of the series.¹⁰

For **2b** and **3b**, the agreement between the experimental isotopic distribution and the statistical model of the [Er_xYb_{2-x}Q₅]⁺ fragment, most likely involving the central metal ion (Figure 2d), indicates that the nitrate anion in the central position can coordinate either erbium or ytterbium regardless of the starting metal salt (see reaction pathway (ii), Scheme 1), proving that ligand scrambling effects take place during the synthesis. Actually, no results on positional control of a specific lanthanide ion over the three available coordination sites have been so far achieved through templating syntheses by using different lanthanide salts as starting materials. Additional attempts made by using acetate or triflate salts of Er³⁺ or Yb³⁺ mixed with two equivalent of Yb³⁺ or Er³⁺ chlorides, respectively, invariably afforded Er_xYb_{3-x}Q₉ complexes as statistical mixtures of homo- and heterometallic species (see Experimental Section). The close similarity of the chemical behavior, reactivity, and size of the two NIR-emissive erbium and ytterbium ions, which can be considered as “vicariants”, leads to similar occupancies of these metal ions over the available coordination sites in the crystal lattice in trinuclear quinolinolato complexes.¹⁰ Scanning electron microscopy (SEM)–energy-dispersive X-ray (EDX) semiquantitative punctual analyses on crystalline samples confirmed the homogeneity of metal distribution with reproducible metal atomic ratios for

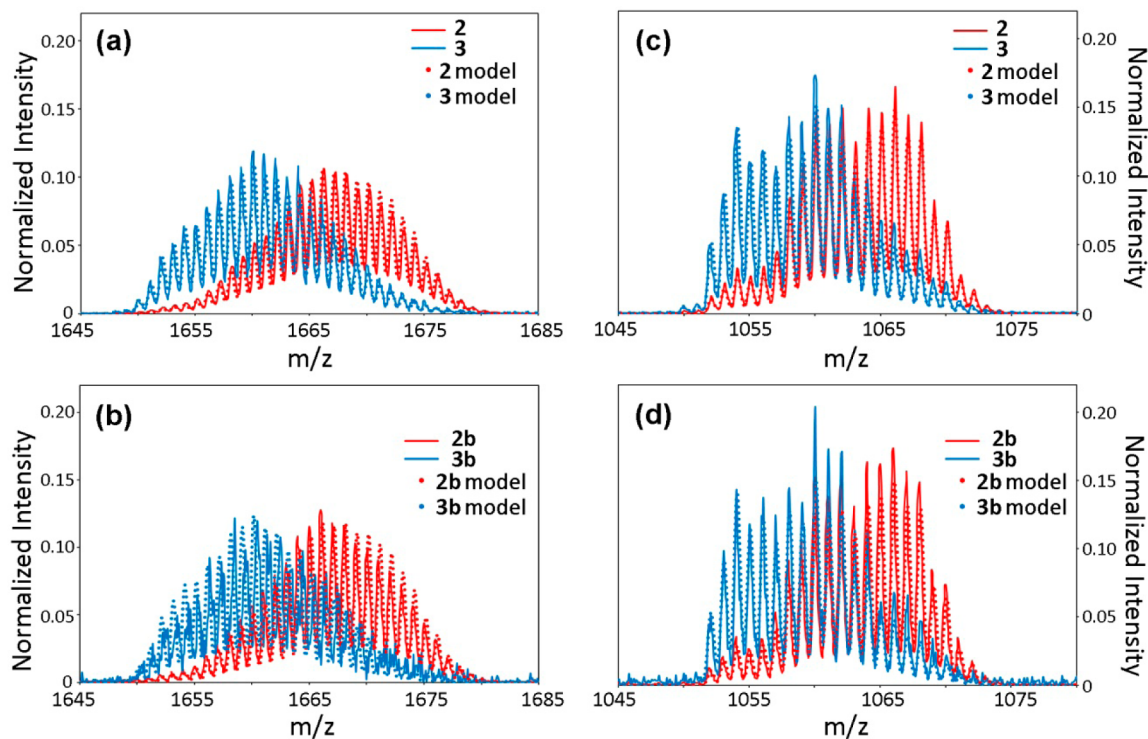


Figure 2. ESI-mass spectra of heterolanthanide compounds, showing the $[\text{Er}_x\text{Yb}_{3-x}\text{Q}_8]^+$ (2–3, panel a; 2b–3b, panel b) and the $[\text{Er}_x\text{Yb}_{2-x}\text{Q}_5]^+$ (2–3, panel c; 2b–3b, panel d) fragments. Dotted lines represent model isotopic distribution functions for a statistical molecular speciation of $\text{Er}_{0.89}\text{Yb}_{2.11}\text{Q}_9$ (2), $\text{Er}_{1.92}\text{Yb}_{1.08}\text{Q}_9$ (3), $\text{Er}_{0.88}\text{Yb}_{2.12}\text{Q}_8\text{NO}_3$ (2b), and $\text{Er}_{1.95}\text{Yb}_{1.05}\text{Q}_8\text{NO}_3$ (3b). Integrated intensities are normalized to unity.

Table 3. Relative Abundances of Molecular Species with Different Er/Yb Atomic Ratios in Heterolanthanide Compounds 2, 3, 2b, and 3b

compound	$\text{Er}_x\text{Yb}_{3-x}$ metal composition			
	$x = 1$	$x = 2$	$x = 0$	$x = 3$
2	44%	18%	35%	3%
2b	44%	18%	35.5%	2.5%
3	25%	44%	5%	26%
3b	24%	44.5%	4%	27.5%

several different crystals (Table S2, Supporting Information). This allows a continuous tuning of the molecular speciation simply by varying the stoichiometry of the metals in the synthesis while ensuring unaltered compositional homogeneity in the sample.

Spectroscopic Studies and Photophysical Properties.

Absorption, solid-state diffuse reflectance (DR), and photoluminescence (PL) spectra in the UV–vis and NIR regions for **1**, **2**, and **3** are reported in Figure 3, whereas corresponding spectra for compounds **1b**, **2b**, and **3b** can be found in Figure S3 in the Supporting Information.

For all the compounds, the absorption spectrum in the visible region is dominated by the typical intense and broad band related to a $\pi-\pi^*$ transition of the quinolinolato ligand with intraligand charge transfer (ILCT) character (Figure 3a).²⁸ In the 800–1800 nm spectral window, DR spectra have been acquired on crystalline samples to avoid interference due to strong solvent absorption (Figure 3b). The narrow bands related to intrashell $f-f$ transitions of Yb^{3+} (${}^2\text{F}_{5/2} \leftarrow {}^2\text{F}_{7/2}$ 1 μm) and Er^{3+} (${}^4\text{I}_{13/2} \leftarrow {}^4\text{I}_{15/2}$ 1.5 μm) are resolved into a fine structure as a consequence of the splitting of the energy levels manifolds due to crystal field effects. These transitions are

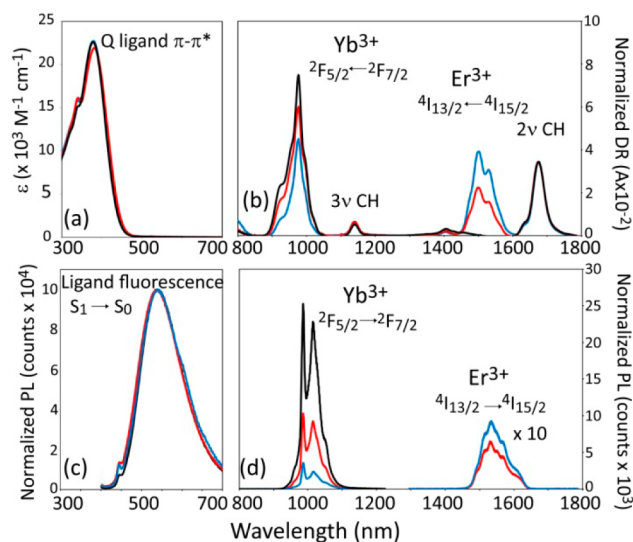


Figure 3. (a) Absorbance spectra in dimethyl sulfoxide (DMSO) solution showing the broad band related to the Q ligand in the UV–vis region; (b) DR spectra of crystalline samples in the vis–NIR region showing lines related to intrashell $f-f$ transitions of Er^{3+} and Yb^{3+} and ligand CH stretching overtones; (c) ligand fluorescence and (d) PL spectra in the NIR region of DMSO solutions excited at $\lambda = 392$ nm. Color coding: **1** (black), **2** (red), and **3** (blue). Spectroscopic labels of Er^{3+} and Yb^{3+} transitions are also indicated. DR spectra are normalized to the 2ν CH band. PL spectra are normalized for absorbed power at excitation wavelength.

particularly sensitive to the chemical coordination environment, and observed bands shapes are slightly different for **1**, **2**, and **3** with respect to compounds **1b**, **2b**, and **3b** (Figure S3b, Supporting Information) where the replacement of the central

Q ligand with a nitrate anion changes the molecular symmetry. The bands at 1680 and 1140 nm in the DR spectra are attributed to the second and third harmonic of the stretching vibration of ligand aromatic CH groups and can serve as useful internal reference for normalizing the spectra of isostructural complexes. DR spectroscopy can therefore be used as a supplementary diagnostic tool for a rough estimation of the amount of erbium and ytterbium ions in the samples through comparison of the intensities of the related integrated peaks.

All the investigated compounds display PL in the visible and in the NIR regions upon single-wavelength irradiation in the ligand lowest absorption band in the near-UV. Broad ligand-centered emission attributed to radiative decay from the excited singlet state S_1 to the ground state S_0 is detected in the green region of the visible spectrum (Figure 3c). Simultaneous PL from Yb^{3+} and Er^{3+} upon single-wavelength irradiation is also observed in the NIR spectral window as a consequence of RET from the excited ligand to the upper energy levels of the lanthanide ions, which become sensitized (Figure 3d). Yb^{3+} ($^2F_{5/2} \rightarrow ^2F_{7/2}$, 1 μm) and Er^{3+} ($^4I_{13/2} \rightarrow ^4I_{15/2}$, 1.5 μm) emission bands are resolved into a fine structure and are Stokes-shifted with respect to DR spectra. The observed NIR-PL spectroscopic features in mixed Er/Yb compounds arise from the contribution of the different species in the samples, where only the fraction of homolanthanide molecular species (Yb_3Q_9 , Er_3Q_9) yields independent emission from the metals, whereas intermetallic communication occurring in heterometallic Er/Yb molecules affects the intensity of the emission bands in the NIR.⁹

A multistep photocycle, involving intraligand, ligand-to-metal, and metal-to-metal energy transfer processes, is in fact responsible for narrow-band lanthanide emission in this class of mixed-lanthanide complexes. This mechanism, which can be simply depicted through a Jablonski diagram, reported in Figure 4, can be briefly summarized as follows. After ligand excitation

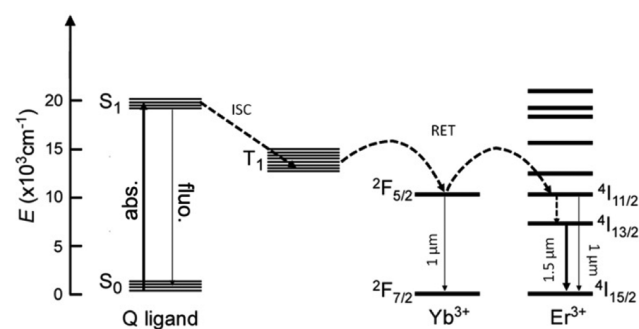


Figure 4. Jablonski diagram depicting the energy levels of the Q ligand, Yb^{3+} , and Er^{3+} ions and the full photocycle in trinuclear quinolinolato complexes. Dashed arrows represent nonradiative processes. Thick arrows indicate the mechanism of Yb-sensitized Er emission in mixed Er/Yb Q-complex. abs. = ligand absorption; fluo. = ligand fluorescence; ISC = intersystem crossing; RET = resonance energy transfer.

in the first singlet excited state S_1 , intersystem crossing (ISC) to excited triplet T_1 becomes competitive with ligand fluorescence ($S_1 \rightarrow S_0$) due to the heavy atom effect induced by coordination to the lanthanide ions. The excited triplet T_1 is then likely to feed, by Förster's RET, the upper energy levels of Yb^{3+} and Er^{3+} . As a consequence of the perfect energy match between the $^2F_{5/2}$ and the $^4I_{11/2}$ levels of Yb^{3+} and Er^{3+} , metal-to-metal

RET can occur between these two ions, which adds a supplementary step to the photocycle.

Advanced time-resolved photophysical studies in the visible and NIR spectral windows have been performed to investigate the most competitive processes that lead to narrow-band NIR emission in heterolanthanide Er/Yb compounds and evaluate their efficiency.

Ligand-Centered Dynamics and Ligand-to-Metal Energy Transfer. Combined transient PL and photoinduced excited-state absorption (ESA) experiments with subpicosecond photoexcitation in the fundamental absorption band of the ligand at 392 nm for **1**, **2**, and **3** in diluted ($\sim 5 \times 10^{-4} \text{M}$) DMSO solution are summarized in Figure 5. Corresponding

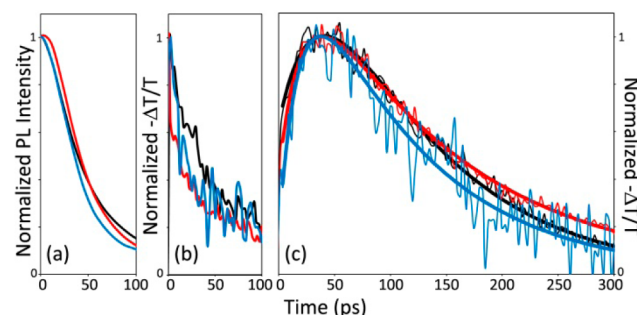


Figure 5. (a) Transient PL in the 400–700 nm region; (b) transient ESA probed in the region 430–440 nm showing ligand singlet decay dynamics and (c) ESA signal attributed to ligand triplet dynamics in the region 560–570 nm and curve fitting (thick lines). Excitation wavelength was $\lambda = 392$ nm. Color coding: **1** (black), **2** (red), and **3** (blue). Signal intensities are normalized to unity.

graphs for **1b**, **2b**, and **3b** are reported in Figure S4 in the Supporting Information. Related time constants for all the investigated compounds are compared in Figure 6.

After photoexcitation, time-resolved PL measurements spectrally integrated over the fluorescence emission spectrum (400–700 nm spectral window) show that the ligand excited state S_1 decays monoexponentially on an ultrafast time scale (Figure 5a). Decay time constants are close to the instrumental temporal resolution limit ($\tau_{\text{fluo}} \approx 50$ ps) for all the investigated

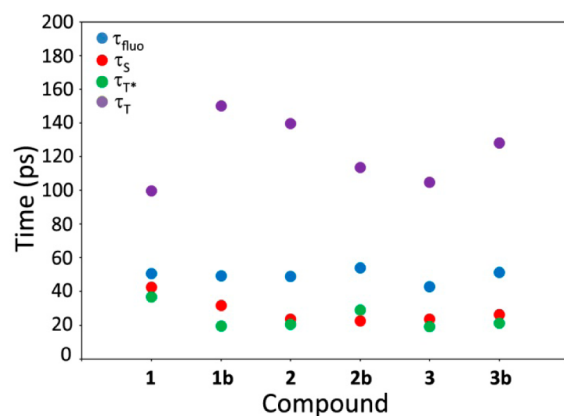


Figure 6. Time constants of the ligand-centered dynamics in the visible spectral region: ligand fluorescence lifetime, τ_{fluo} , blue dots; excited singlet decay time constant from ESA experiments, τ_S , red dots; excited triplet rise time, τ_{T^*} , green dots; and excited triplet decay time, τ_T , purple dots, as retrieved from ESA experiments. Errors fall in the range 0.4–7 ps (see Table S3, Supporting Information).

compounds (Figure 6), as expected for this class of complexes, where the presence of the heavy lanthanide ion favors the intraligand ISC mechanism.^{16,17} ESA experiments probed in the 430–440 nm spectral window (Figure 5b) show signals attributable to excited singlet, with prompt risetimes followed by ultrafast relaxation. Singlet decay occurs with time constants (τ_s) in agreement with the resolution limited ones retrieved from transient PL (see Figure 6). When the 560–570 nm region, where the singlet signal is almost undetectable, is probed, the dynamics related to ligand triplet excited states can be determined (Figure 5c). Triplet population shows an ultrafast activation complementary to the excited singlet decay, with similar time constants that can be reliably attributed to the singlet→triplet intersystem crossing process (τ_{T^*} , Figure 6). Triplet decay is ultrafast, and curve fitting yields triplet lifetimes (τ_T) in the range 100–150 ps (Figure 6), in agreement with previous reports for erbium and ytterbium quinolinolate complexes.^{16,17} By comparing these findings with the $\tau_T = 1.4$ ns value previously found for the analogous Gd_3Q_9 complex,^{16,17} where upper gadolinium levels lie too high in energy to be fed through indirect excitation from the ligand, it can be deduced that the excited triplet is strongly quenched by ligand-to-metal energy transfer. Therefore, lanthanide sensitization is extremely efficient in all the investigated compounds. The triplet lifetime can then be considered as the time constant of the ligand-to-metal RET process. Time constants and related experimental errors, details of kinetic equations, and curve fitting procedure are reported in the Supporting Information.

Metal-Centered Dynamics and Metal-to-Metal Energy Transfer. Time-resolved PL studies showing the metal-centered dynamics in the NIR spectral region for **1**, **2**, and **3** in diluted ($\sim 5 \times 10^{-4}$ M) DMSO solution are summarized in Figure 7.

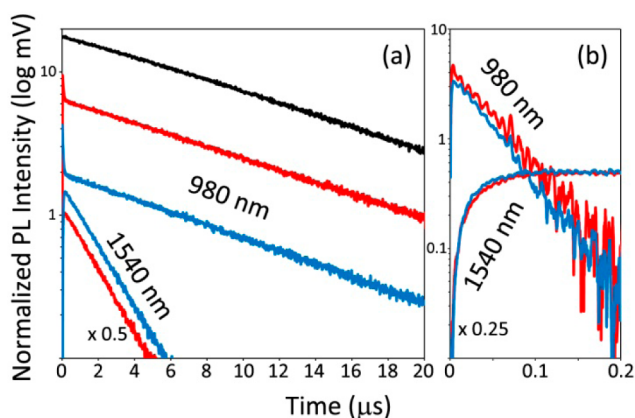


Figure 7. (a) NIR decay dynamics of **1** (black), **2** (red), and **3** (blue) at 980 and 1540 nm. (b) NIR dynamics on a short time scale of **2** (red) and **3** (blue): decay traces at 980 nm and at 1540 nm have been obtained by subtracting the long-lived component attributed to Yb_3Q_9 and the Er_3Q_9 contribution, respectively. Signal intensities are plotted on a logarithmic scale. Excitation wavelength was 392 nm. Intensities are normalized for absorbed power at excitation wavelength.

Corresponding data for **1b**, **2b**, and **3b** are reported in Figure S5 in the Supporting Information. Figure 8 summarizes the decay time constants for the Er^{3+} and Yb^{3+} dynamics for all the investigated compounds.

A monoexponential decay, related to $Yb^{3+} {}^2F_{5/2} \rightarrow {}^2F_{7/2}$ emission at 980 nm, is detected for **1** (black line, Figure 7a) with a time constant $\tau_{Yb} \approx 11 \mu s$ (Figure 8). For the mixed Er–

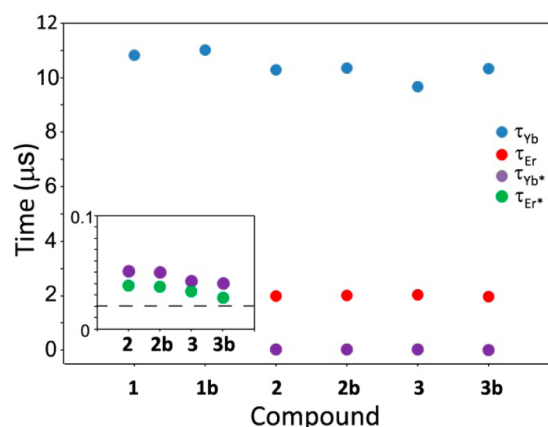


Figure 8. Time constants of the metal-centered dynamics in the NIR spectral region: ytterbium decay time for radiative emission at 980 nm, τ_{Yb} , blue dots; erbium emission decay time at 1540 nm, τ_{Er} , red dots; time constant of the Yb-to-Er RET, τ_{Yb^*} , purple dots; erbium signal rise time at 1540 nm, τ_{Er^*} , green dots. Dashed line in the inset represents erbium signal rise time at 1540 nm in Er_3Q_9 . Errors fall in the range 0.4–10 ns (see Table S4, Supporting Information).

Yb compounds **2** and **3**, two distinct decay dynamics are observed at 980 and 1540 nm due to the coexistence of Yb^{3+} and Er^{3+} in the samples (Figure 7a, **2**, red line; **3**, blue line). The signal at 1540 nm arises from erbium ${}^4I_{13/2} \rightarrow {}^4I_{15/2}$ radiative emission and decays monoexponentially for both **2** and **3** with the same dynamics as Er_3Q_9 ^{9,12} ($\tau_{Er} \approx 2 \mu s$, red dots, Figure 8). As described in Figure 4, this emission is most likely consequent to the population of the erbium ${}^4I_{13/2}$ level after nonradiative cascade from the upper lying ${}^4I_{9/2}$ level. The difference of 1540 nm signal intensities between **2** and **3** reflects the composition of the two samples (Table 3) and, in particular, the amount of Yb_3Q_9 not giving rise to emission at 1540 nm. Instead, for the decay trace at 980 nm, two components are clearly distinguishable with lifetimes differing for almost three orders of magnitude, as retrieved by double-exponential fitting. The longer-lived component, showing similar dynamics to **1** ($\tau_{Yb} \approx 10 \mu s$, blue dots, Figure 8) can be attributed to $Yb^{3+} {}^2F_{5/2} \rightarrow {}^2F_{7/2}$ emission from the fraction of Yb_3Q_9 species present in the two samples and can be weighted accordingly (Table 3). Conversely, the ultrafast decay component is likely due to the strong quenching of ytterbium ${}^2F_{5/2}$ level induced by resonant Yb-to-Er (${}^2F_{5/2} \rightarrow {}^4I_{9/2}$) energy transfer, as depicted in Figure 4.⁹ This observation becomes more evident from a closer inspection of the ytterbium and erbium dynamics on a shorter time scale as reported in Figure 7, panel b, where the contributions of Yb_3Q_9 and Er_3Q_9 fractions in the two samples are subtracted from the signals at 980 and 1540 nm, respectively (see Figure S6, Supporting Information for details). Therefore, the resulting components are to be solely attributed to the “pure” heterometallic Er/Yb species. The erbium signal rising at 1540 nm appears to be complementary to the ytterbium decay at 980 nm, in good agreement with the dynamics expected on the basis of a Yb-to-Er RET. This is further corroborated by the comparison of related time constants in the inset of Figure 8 (980 nm decay time, τ_{Yb^*} , purple dots; 1540 nm rise time, τ_{Er^*} , green dots) that fall in the 30–50 ns range for all the investigated compounds.

The dynamics of the process leading to erbium ${}^4I_{13/2}$ population is therefore ultrafast, and noteworthy, it is slightly slower than that observed in the homometallic Er_3Q_9 complex

($\tau = 21$ ns, dashed line in the inset of Figure 8) as a consequence of the direct involvement of excited Yb^{3+} in the Er^{3+} sensitization mechanism in heterolanthanide species.⁹ The shortening of intermetallic distances in **2b** and **3b** with respect to **2** and **3** seems to lead to a slightly faster trend in Yb-to-Er RET dynamics. However, the small differences in the donor–acceptor separation, which is well below the Förster’s radius ($R_0 \approx 10$ Å) in all the investigated compounds, fall beyond any possible discrimination of related quantum efficiencies on the basis of the Förster’s theory.⁹

Moreover, the corrected signals at 1540 nm for compounds **2** and **3** in Figure 7, panel b (and **2b–3b**, Figure S5b, Supporting Information) are of the same intensity, which suggests that erbium sensitization in heterometallic species is quantitative and independent of the number of erbium ions in the samples when exciting in a linear regime of 0.1 excitations per complex.⁹

The efficiency of the metal-to-metal resonant energy transfer (η_{RET}) can be easily estimated by taking into account the decay time of the donor (Yb^{3+}) in the absence (τ_{Yb}) and in the presence (τ_{Yb^*}) of the acceptor (Er^{3+}), by considering the latter parameter as the time constant of Yb-to-Er RET, according to the following equation:

$$\eta_{\text{RET}} = \frac{1}{1 + \frac{\tau_{\text{Yb}^*}}{\tau_{\text{Yb}}}}$$

Therefore, almost quantitative ($\sim 99.5\%$) Yb-to-Er RET efficiency is found for all the heterolanthanide complexes investigated in this work thanks to the short intermetallic distances in the trinuclear molecular framework (< 3.5 Å).^{10,12–15}

Energy back transfer from Er to Yb is prevented by the ultrashort lifetime of the $\text{Er}^4\text{I}_{11/2}$ level as observed in Er_3Q_9 (17 ns).⁹ From all these considerations, it is then possible to conclude that in heterolanthanide Er–Yb molecular assemblies, where the two lanthanide ions are held at a short distance between each other, Yb-to-Er RET is strongly favored and takes place as the only competitive mechanism leading to erbium $^4\text{I}_{13/2} \rightarrow ^4\text{I}_{15/2}$ emission as the final step.

As a final remark, it is interesting to note that no significant differences in ytterbium (or erbium) luminescence lifetimes are found for **1** and **1b** (**2**, **3** and **2b**, **3b**) in DMSO solution despite the replacement of one Q ligand with the nitrate anion and therefore the lower number of CH groups, which are known to act as efficient vibrational quenchers toward NIR emitters.^{29–31} For crystalline samples of **1** and **1b**, where solvent effects are ruled out, the observed emission lifetime at 980 nm, τ_{Yb} (**1b**) = 11.29 μs , is noticeably longer than τ_{Yb} (**1**) = 10.10 μs (see Figure S7, Supporting Information), in agreement with the lower number of CH quenchers (48 vs 54). In solution, this observation may be hampered by the lability of the bond at the central ligand, which may be likely replaced by coordinating DMSO molecules.

Decay constants with related experimental errors and curve fitting procedures are reported in the Supporting Information.

Er/Yb-Doped Silica Thin Films. To investigate the processing potential of heterolanthanide Er/Yb quinolinolato complexes, experiments on the incorporation of compound **2** into silica thin films have been performed. Homogeneous and transparent doped thin films have been prepared by dipcoating or dropcasting a *sol* solution, containing a mixture of alkoxysilane precursors and the complex dissolved in ethanol on a quartz support. Different alkoxysilanes (glycidoxy-propyl-

trimethoxy-silane, GLYMO, and a mixture of tetramethoxysilane, TMOS, and isobutyl-trimethoxy-silane, ITMS, see Experimental Section) have been used as starting precursors to investigate potential matrix effects on the optical properties of the final material.

The best results in terms of optical response have been obtained when using GLYMO as precursor, and corresponding NIR PL spectra and dynamics are reported in Figure 9. The

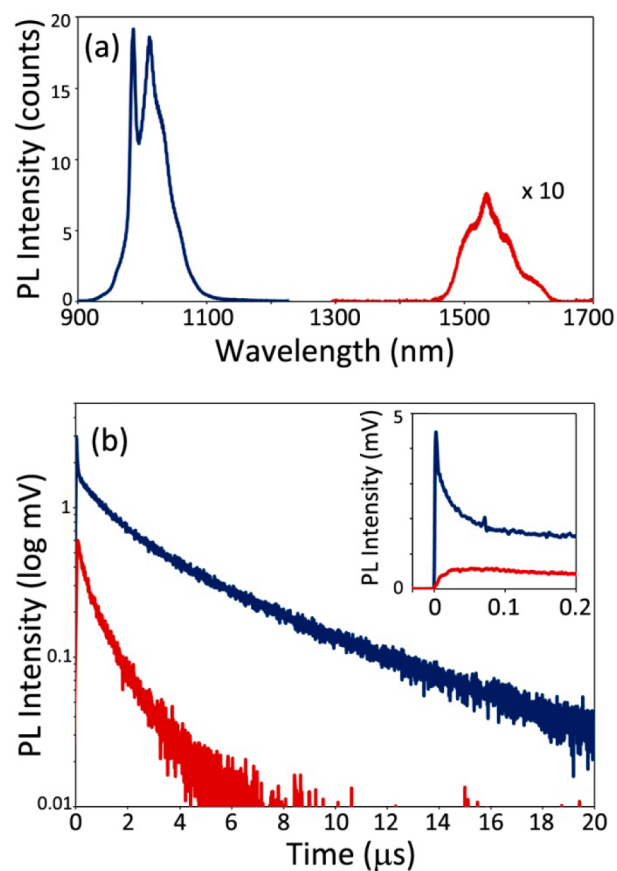


Figure 9. NIR PL studies of a GLYMO-based silica thin film doped with **2**: (a) PL spectrum showing the emission bands related to $\text{Yb}^{3+} {}^2\text{F}_{5/2} \rightarrow {}^2\text{F}_{7/2}$ (blue) and $\text{Er}^{3+} {}^4\text{I}_{13/2} \rightarrow {}^4\text{I}_{15/2}$ (red) transitions; (b) NIR dynamics at 980 nm (blue) and 1540 nm (red) plotted on a logarithmic scale. In the inset of panel b, signal intensities in the 0–200 ns time range are reported on a linear scale. Excitation wavelength was 355 nm.

doped GLYMO-based film retains the main optical properties of **2**, showing dual NIR luminescence at 1 and 1.5 μm , after photoexcitation at 355 nm. The spectral profiles of Yb^{3+} and Er^{3+} emissions, shown in Figure 9, panel a (blue line, Yb^{3+} , red line, Er^{3+}), are very similar to those observed for **2** in solution (Figure 3d). This indicates that the coordination sphere of both ions, and consequently the molecular framework, remains mostly unaltered as the complex is embedded into the silica host matrix. The NIR emission dynamics, shown in Figure 9, panel b, confirms that Yb-to-Er RET still takes place in the doped film, as evidenced by the ultrafast component of the Yb^{3+} 980 nm decay trace (see inset of Figure 9b, blue line). The longer-lived fraction of the 980 nm decay has a double-exponential dynamics, and curve fitting yields the following time constants: $\tau_{\text{Yb1}} = 1.48$ μs (60%) and $\tau_{\text{Yb2}} = 6.57$ μs (40%). Similar observations can be made for the Er^{3+} decay at 1540 nm

(red line, Figure 9), for which $\tau_{\text{Er1}} = 0.41 \mu\text{s}$ (60%) and $\tau_{\text{Er2}} = 1.81 \mu\text{s}$ (40%) are retrieved from double-exponential fitting. These results seem to suggest that two different populations of complexes exist in the host matrix, whose luminescence lifetimes are slightly shortened to different extent by second sphere quenching interactions with the silica backbone, as already observed for an analogous Yb quinolinolate-doped silica–glass material.²¹ It must be remarked that repeated measurements have shown that the same optical features are flawlessly reproduced throughout the film, which prove the optimal dispersion of the dopant compound in the silica matrix.

Data for the TMOS/ITMS-based film are summarized in Figure S8 in the Supporting Information. Further investigations on the effects of silica matrices based on different alkoxy silane precursors on the optical/photophysical properties of thin films incorporating NIR emitting lanthanide complexes are currently being performed in our laboratories.

CONCLUSIONS

In conclusion, we have reported a detailed combined chemical/photophysical study on a series of trinuclear homo- (Yb) and heterolanthanide (Er, Yb) quinolinolato complexes as promising optically active components of Er/Yb codoped NIR-emissive materials. Depending on the starting metal salts used in the synthesis, homoleptic complexes of general formula $\text{Er}_x\text{Yb}_{3-x}\text{Q}_9$ ($x = 0, 1; x = 1, 2; x = 2, 3$; chloride, acetate, or triflate salts) and the corresponding heteroleptic complexes $\text{Er}_x\text{Yb}_{3-x}\text{Q}_8\text{NO}_3$ ($x = 0, 1\mathbf{b}; x = 1, 2\mathbf{b}; x = 2, 3\mathbf{b}$; mixture of chloride and nitrate salts) have been synthesized and characterized. XRD structural studies on $\mathbf{1b}$ have shown that this complex has a trinuclear $\text{Yb}_3\text{Q}_8\text{NO}_3$ molecular arrangement, where the central ytterbium is chelated by a nitrate anion allowing a remarkable shortening of intermetallic distances with respect to the Yb_3Q_9 analog. Metal compositional analysis on the heterometallic compounds, performed by ICP–mass measurements, has evidenced metal ratios close to the expected ones on the basis of the stoichiometric amounts used in the synthesis, with only a slightly favored affinity (2–4%) of Yb^{3+} with respect to Er^{3+} upon coordination to the Q ligand. Model analysis of ESI–mass spectra shows that for the mixed metal compounds $\mathbf{2}$, $\mathbf{2b}$, $\mathbf{3}$, and $\mathbf{3b}$, the relative abundance of heterometallic Er/Yb molecular species with respect to the homometallic ones is consistent with predictions made on the basis of the relative amounts of Er^{3+} and Yb^{3+} ions in each sample, statistically distributed over the molecular coordination sites. These observations point out the “vicariant” chemical behavior of ytterbium and erbium ions toward coordination regardless of the starting metal salt used in the synthetic procedure and that molecular speciation can be varied according to the metal stoichiometry established in the experimental design.

Spectroscopic and time-resolved photophysical studies in the visible and NIR spectral regions have allowed a full disclosure of the photocycle leading to narrow-band lanthanide emission in these systems. Ligand-centered dynamics in the visible has been studied by means of time-resolved PL and photoinduced absorption experiments, which have confirmed that the Q ligand is able to sensitize Yb^{3+} and Er^{3+} with high efficiency through a two-step mechanism involving excited triplet levels. Mixed Er/Yb compounds show simultaneous dual luminescence at 1 and 1.5 μm upon single-wavelength irradiation in the ligand lowest absorption band as a result of the weighted contribution of the different hetero- and homometallic species

in the samples. These spectral features can therefore be finely modulated by tuning the molecular speciation simply on variation of the Er/Yb metal ratio. Time-resolved studies in the NIR region provide evidence that the excited Yb^{3+} is directly quenched by RET to Er^{3+} and that this process is favored by the shorter intermetallic distances in heteroleptic complexes. Yb-to-Er RET is quantitative, and emission intensity at 1540 nm is independent of the number of erbium ions in the sample.

In the solid state, a noticeable increase of the Yb^{3+} emission lifetime is observed in the heteroleptic $\mathbf{1b}$ complex with respect to the homoleptic analog $\mathbf{1}$ as a consequence of the lowering of the number of CH quenching groups in the surroundings of the emitting lanthanide ion. ESI–mass spectrometry provided evidence that the trinuclear structure is preserved in solution as $[\text{Er}_x\text{Yb}_{3-x}\text{Q}_8]^+$ ($x = 0–3$) species likely resulting from the fragmentation of the labile central coordinated ligand.

Finally, it has been demonstrated that these kinds of complexes can be easily processed through mild solution techniques, such as the sol–gel method, without alterations. Highly transparent and homogeneous silica thin films doped with $\mathbf{2}$ have been prepared, which show the same optical properties of the incorporated complex in solution. This strategy opens new perspectives for the development of NIR-emitting codoped Er/Yb materials such as optical waveguides and amplifiers, while it takes advantage of the effective molecular approach for the control of light conversion processes in functional heterolanthanide assemblies.

EXPERIMENTAL SECTION

General. All the reagents and solvents were purchased from Aldrich and used without further purification.

Syntheses. *Synthesis of 1 and 1b.* A few drops of NH_3 28% up to a final concentration of $2.0 \times 10^{-2} \text{ mol dm}^{-3}$ ($\text{pH} \cong 10$) were added to a suspension of 8-hydroxy-quinoline (0.145 g, 1 mmol) in H_2O (100 mL) under stirring. After 30 min, a water solution of $\text{YbCl}_3 \cdot 6\text{H}_2\text{O}$ ($\mathbf{1}$, 0.129 g, 0.33 mmol) or $\text{Yb}(\text{NO}_3)_3 \cdot 6\text{H}_2\text{O}$ ($\mathbf{1b}$, 0.154 g, 0.33 mmol) was added to the above mixture, which was allowed to react for 2 days until the white solid due to the unreacted ligand disappeared. A yellow precipitate formed, which was collected by filtration, washed with water, NaOH 0.1 M, water, and dried in oven at 60 °C overnight (almost quantitative yield). The solid was then dissolved in warm CH_3CN , the solvent was rotoevaporated to incipient precipitation, and after several days, yellow microcrystals of $\mathbf{1}$ and $\mathbf{1b}$ were obtained. XRD data were collected on single crystals of $\mathbf{1b}$ for structural studies. Analytical and spectroscopic data for $\mathbf{1}$. CHN Found (Calculated for $\text{C}_{81}\text{H}_{54}\text{Yb}_3\text{N}_9\text{O}_9 \cdot 3\text{H}_2\text{O}$): C% 52.18 (52.01), H% 3.35 (3.23), N% 6.82 (6.74). FT-IR, cm^{-1} : 3047 m, 1601 m, 1571 s, 1498 vs, 1466 vs, 1424 mw, 1383 s, 1318 s, 1276 m, 1231 m, 1174 w, 1109 vs, 1035 w, 907 w, 823 m, 804 m, 788 m, 732 s, 648 m, 607 m, 592 w; 571 w, 504 m, 490 m, 458 w, 419 mw, 397 m, 384 m, 376 m, 353 m, 335 vw, 326 w, 315 vw, 303 w, 290 w, 280 m, 266 w, 253 m, 247 m, 226 m, 203 m, 177 m, 151 ms, 140 m, 132 m, 121 m, 101m 90 m 80 mw, 74 mw, 57 mw. UV–vis–NIR absorption, nm , $[\text{mol}^{-1} \text{ dm}^3 \text{ cm}^{-1}]$, DMSO: 381 $[2.25 \times 10^4]$, 977 ($\text{Yb}^{3+} {}^2\text{F}_{5/2} \leftarrow {}^2\text{F}_{7/2}$) $[20]$. DR, nm: 262, 344, 385; 928, 952, 979 (${}^2\text{F}_{7/2} \leftarrow {}^2\text{F}_{5/2}$), 1147 ($3\nu\text{C–H}$), 1678 ($2\nu\text{C–H}$). ESI–mass ($\text{CH}_3\text{CN}/\text{CH}_3\text{OH}$ 3/1), m/z : 1671.87 $[\text{Yb}_3\text{Q}_8]^+$. Analytical and spectroscopic data for $\mathbf{1b}$. CHN Found (Calculated for $\text{C}_{72}\text{H}_{48}\text{Yb}_3\text{N}_9\text{O}_{11} \cdot 3\text{H}_2\text{O}$): C% 47.75 (48.36), H% 3.25 (3.04), N% 7.14 (7.05). FT-IR, cm^{-1} : 3047 m, 1601 m, 1571 s, 1498 vs, 1466 vs, 1424 mw, 1383 s, 1318 s, 1276 m, 1231 m, 1174 w, 1109 vs, 1035 w, 907 w, 823 m, 804 m, 788 m, 732 s, 648 m, 607 m, 592 w; 571 w, 504 m, 490 m, 458 w, 419 mw. UV–vis–NIR absorption, nm , $[\text{mol}^{-1} \text{ dm}^3 \text{ cm}^{-1}]$, DMSO: 378 $[2.06 \times 10^4]$, 977 ($\text{Yb}^{3+} {}^2\text{F}_{5/2} \leftarrow {}^2\text{F}_{7/2}$). DR, nm: 262, 344, 385; 928, 952, 979 ($\text{Yb}^{3+} {}^2\text{F}_{7/2} \leftarrow {}^2\text{F}_{5/2}$), 1147 ($3\nu\text{C–H}$), 1678 ($2\nu\text{C–H}$). ESI–mass ($\text{CH}_3\text{CN}/\text{CH}_3\text{OH}$ 3/1), m/z : 1671.87 $[\text{Yb}_3\text{Q}_8]^+$.

Synthesis of 2, 3, 2b, and 3b. Syntheses were carried out following the same procedure described for **1** and **1b** by adding to a solution containing 1 mmol of the deprotonated ligand, a mixture of 0.22 mmol of $\text{LnCl}_3 \cdot 6\text{H}_2\text{O}$ ($\text{Ln} = \text{Yb}$, **2**, **2b**; Er , **3**, **3b**) and 0.11 mmol of $\text{LnCl}_3 \cdot 6\text{H}_2\text{O}$ ($\text{Ln} = \text{Er}$, **2**; Yb , **3**) or $\text{Ln}(\text{NO}_3)_3 \cdot 6\text{H}_2\text{O}$ ($\text{Ln} = \text{Er}$, **2b**; Yb , **3b**) in water. A yellow precipitate formed, and it was then collected by filtration, washed with water, NaOH 0.1 M, water, and dried in oven at 60 °C overnight (yield > 95%). Yellow microcrystals were obtained after recrystallization from CH_3CN . Analytical and spectroscopic data for **2**. CHN Found (Calculated for $\text{C}_{81}\text{H}_{54}\text{ErYb}_2\text{N}_9\text{O}_9 \cdot 3\text{H}_2\text{O}$): C% 52.25 (52.17), H% 3.38 (3.24), N% 6.87 (6.76). FT-IR, cm^{-1} : 3047 m, 1601 m, 1571 s, 1498 vs, 1466 vs, 1424 mw, 1383 s, 1318 s, 1276 m, 1231 m, 1174 w, 1109 vs, 1035 w, 907 w, 823 m, 804 m, 788 m, 732 s, 648 m, 607 m, 592 w; 571 w, 504 m, 489 m, 458 w, 419 mw, 397 m, 384 m, 377 m, 353 m, 335 vw, 326 w, 315 vw, 303 w, 289 w, 280 m, 267 w, 253 m, 247 m, 226 m, 203 m, 177 m, 151 ms, 140 m, 132 m, 121 m, 105 m, 101 m, 89 m, 80 mw, 74 mw, 57 mw. UV-vis-NIR absorption, nm , $[\text{mol}^{-1} \text{dm}^3 \text{cm}^{-1}]$, DMSO: 379 $[2.20 \times 10^4]$, 522 ($\text{Er}^{3+} {}^2\text{H}_{11/2} \leftarrow {}^4\text{I}_{15/2}$), 652 ($\text{Er}^{3+} {}^4\text{F}_{9/2} \leftarrow {}^4\text{I}_{15/2}$), 977 ($\text{Yb}^{3+} {}^2\text{F}_{5/2} \leftarrow {}^2\text{F}_{7/2}$ and $\text{Er}^{3+} {}^4\text{I}_{11/2} \leftarrow {}^4\text{I}_{15/2}$) [20], 1540 ($\text{Er}^{3+} {}^4\text{I}_{13/2} \leftarrow {}^4\text{I}_{15/2}$) [3.5]. DR, nm: 262, 344, 385, 521 ($\text{Er}^{3+} {}^2\text{H}_{11/2} \leftarrow {}^4\text{I}_{15/2}$), 653 ($\text{Er}^{3+} {}^4\text{F}_{9/2} \leftarrow {}^4\text{I}_{15/2}$), 802 ($\text{Er}^{3+} {}^4\text{I}_{4/2} \leftarrow {}^4\text{I}_{15/2}$), 979 ($\text{Yb}^{3+} {}^2\text{F}_{5/2} \leftarrow {}^2\text{F}_{7/2}$ and $\text{Er}^{3+} {}^4\text{I}_{11/2} \leftarrow {}^4\text{I}_{15/2}$), 1147(3 ν C-H), 1533 ($\text{Er}^{3+} {}^4\text{I}_{13/2} \leftarrow {}^4\text{I}_{15/2}$), 1678 (2 ν C-H). ICP-mass (atomic ratios, average on five repeated measurements): Er/Yb 1:2.36. ESI-mass ($\text{CH}_3\text{CN}/\text{CH}_3\text{OH}$ 3/1), m/z : 1666.5 $[\text{ErYb}_2\text{Q}_8]^+$. The same product was obtained when two equivalents of Yb^{3+} chloride were reacted with one equivalent of Er^{3+} acetate or triflate. Analytical and spectroscopic data for **3**. CHN Found (Calculated for $\text{C}_{81}\text{H}_{54}\text{Er}_2\text{YbN}_9\text{O}_9 \cdot 3\text{H}_2\text{O}$): C% 51.80 (52.33), H% 3.34 (3.25), N% 6.60 (6.78). FT-IR, cm^{-1} : 3047 m, 1602 m, 1570 s, 1498 vs, 1466 vs, 1425 mw, 1383 s, 1318 s, 1278 m, 1232 m, 1173 w, 1109 vs, 1035 w, 907 w, 824 m, 804 m, 788 m, 732 s, 648 m, 607 m, 592 w; 571 w, 504 m, 489 m, 458 w, 419 mw. UV-vis-NIR absorption, nm , $[\text{mol}^{-1} \text{dm}^3 \text{cm}^{-1}]$, DMSO: 381 $[2.25 \times 10^4]$, 522 ($\text{Er}^{3+} {}^2\text{H}_{11/2} \leftarrow {}^4\text{I}_{15/2}$), 652 ($\text{Er}^{3+} {}^4\text{F}_{9/2} \leftarrow {}^4\text{I}_{15/2}$), 977 ($\text{Yb}^{3+} {}^2\text{F}_{5/2} \leftarrow {}^2\text{F}_{7/2}$ and $\text{Er}^{3+} {}^4\text{I}_{11/2} \leftarrow {}^4\text{I}_{15/2}$). DR, nm: 262, 344, 385, 521 ($\text{Er}^{3+} {}^2\text{H}_{11/2} \leftarrow {}^4\text{I}_{15/2}$), 653 ($\text{Er}^{3+} {}^4\text{F}_{9/2} \leftarrow {}^4\text{I}_{15/2}$), 802 ($\text{Er}^{3+} {}^4\text{I}_{4/2} \leftarrow {}^4\text{I}_{15/2}$), 979 ($\text{Yb}^{3+} {}^2\text{F}_{5/2} \leftarrow {}^2\text{F}_{7/2}$ and $\text{Er}^{3+} {}^4\text{I}_{11/2} \leftarrow {}^4\text{I}_{15/2}$), 1147(3 ν C-H), 1533 ($\text{Er}^{3+} {}^4\text{I}_{13/2} \leftarrow {}^4\text{I}_{15/2}$), 1678 (2 ν C-H). ICP-mass (atomic ratios, average on five repeated measurements): Er/Yb 1:0.56. ESI-mass ($\text{CH}_3\text{CN}/\text{CH}_3\text{OH}$ 3/1), m/z : 1660.1 $[\text{Er}_2\text{YbQ}_8]^+$. The same product was obtained when two equivalents of Er^{3+} chloride were reacted with one equivalent of Yb^{3+} acetate or triflate. Analytical and spectroscopic data for **2b**. CHN Found (Calculated for $\text{C}_{72}\text{H}_{48}\text{ErYb}_2\text{N}_9\text{O}_{11} \cdot 3\text{H}_2\text{O}$): C% 49.77 (48.51), H% 2.82 (3.05), N% 6.44 (7.07). FT-IR, cm^{-1} : 3049 m, 1602 m, 1571 s, 1499 vs, 1466 vs, 1423 mw, 1382 s, 1318 s, 1277 m, 1230 m, 1173 w, 1109 vs, 1036 w, 908 w, 822 m, 804 m, 788 m, 732 s, 649 m, 606 m, 590 w; 571 w, 504 m, 490 m, 457 w, 420 mw. UV-vis-NIR absorption, nm , $[\text{mol}^{-1} \text{dm}^3 \text{cm}^{-1}]$, DMSO: 378 $[2.09 \times 10^4]$, 522 ($\text{Er}^{3+} {}^2\text{H}_{11/2} \leftarrow {}^4\text{I}_{15/2}$), 652 ($\text{Er}^{3+} {}^4\text{F}_{9/2} \leftarrow {}^4\text{I}_{15/2}$), 977 ($\text{Yb}^{3+} {}^2\text{F}_{5/2} \leftarrow {}^2\text{F}_{7/2}$ and $\text{Er}^{3+} {}^4\text{I}_{11/2} \leftarrow {}^4\text{I}_{15/2}$). DR, nm: 262, 344, 385, 521 ($\text{Er}^{3+} {}^2\text{H}_{11/2} \leftarrow {}^4\text{I}_{15/2}$), 653 ($\text{Er}^{3+} {}^4\text{F}_{9/2} \leftarrow {}^4\text{I}_{15/2}$), 802 ($\text{Er}^{3+} {}^4\text{I}_{4/2} \leftarrow {}^4\text{I}_{15/2}$), 979 ($\text{Yb}^{3+} {}^2\text{F}_{5/2} \leftarrow {}^2\text{F}_{7/2}$ and $\text{Er}^{3+} {}^4\text{I}_{11/2} \leftarrow {}^4\text{I}_{15/2}$), 1147 (3 ν C-H), 1533 ($\text{Er}^{3+} {}^4\text{I}_{13/2} \leftarrow {}^4\text{I}_{15/2}$), 1678 (2 ν C-H). ICP-mass (atomic ratios, average on five repeated measurements): Er/Yb 1:2.44. ESI-mass ($\text{CH}_3\text{CN}/\text{CH}_3\text{OH}$ 3/1), m/z : 1666.5 $[\text{ErYb}_2\text{Q}_8]^+$. Analytical and spectroscopic data for **3b**. CHN Found (Calculated for $\text{C}_{72}\text{H}_{48}\text{Er}_2\text{YbN}_9\text{O}_{11} \cdot 3\text{H}_2\text{O}$): C% 49.23 (48.67), H% 2.81 (3.06), N% 6.62 (7.09). FT-IR, cm^{-1} : 3048 m, 1602 m, 1571 s, 1499 vs, 1466 vs, 1423 mw, 1382 s, 1318 s, 1277 m, 1230 m, 1171 w, 1109 vs, 1036 w, 909 w, 822 m, 804 m, 787 m, 732 s, 650 m, 606 m, 590 w; 571 w, 504 m, 490 m, 457 w, 420 mw. UV-vis-NIR absorption, nm , $[\text{mol}^{-1} \text{dm}^3 \text{cm}^{-1}]$, DMSO: 378 $[2.06 \times 10^4]$, 522 ($\text{Er}^{3+} {}^2\text{H}_{11/2} \leftarrow {}^4\text{I}_{15/2}$), 652 ($\text{Er}^{3+} {}^4\text{F}_{9/2} \leftarrow {}^4\text{I}_{15/2}$), 977 ($\text{Yb}^{3+} {}^2\text{F}_{5/2} \leftarrow {}^2\text{F}_{7/2}$ and $\text{Er}^{3+} {}^4\text{I}_{11/2} \leftarrow {}^4\text{I}_{15/2}$). DR, nm: 262, 344, 385, 521 ($\text{Er}^{3+} {}^2\text{H}_{11/2} \leftarrow {}^4\text{I}_{15/2}$), 653 ($\text{Er}^{3+} {}^4\text{F}_{9/2} \leftarrow {}^4\text{I}_{15/2}$), 802 ($\text{Er}^{3+} {}^4\text{I}_{4/2} \leftarrow {}^4\text{I}_{15/2}$), 979 ($\text{Yb}^{3+} {}^2\text{F}_{5/2} \leftarrow {}^2\text{F}_{7/2}$ and $\text{Er}^{3+} {}^4\text{I}_{11/2} \leftarrow {}^4\text{I}_{15/2}$), 1147 (3 ν C-H), 1533 ($\text{Er}^{3+} {}^4\text{I}_{13/2} \leftarrow {}^4\text{I}_{15/2}$), 1678 (2 ν C-H). ICP-mass (atomic ratios, average on five repeated measure-

ments): Er/Yb 1:0.54. ESI-mass ($\text{CH}_3\text{CN}/\text{CH}_3\text{OH}$ 3/1), m/z : 1660.1 $[\text{Er}_2\text{YbQ}_8]^+$.

Preparation of Silica Thin Films Doped with 2. GLYMO Thin Film. The sol precursor was prepared by mixing GLYMO with EtOH and H_2O (molar ratio = 1:9:5) under stirring at room temperature (RT) for 24 h. Subsequently, a volume of 2.5 mL of **2** in EtOH (5×10^{-4} M) was added to 7.5 mL of the sol precursor, and the mixture was maintained under stirring at 50 °C for 1 h. Transparent sol was obtained. Films were prepared by the dip coating or drop casting method. After preparation, all films were dried at room temperature for 48 h. Quartz slides were employed as substrates for film preparation. Before coating, the substrates were cleaned through water soap, distilled water, acetone, and finally rinsed with isopropanol. PL measurements have been performed on dropcasted films.

TMOS/ITMS Thin Film. The precursor sol solution was prepared by mixing 8 mL of absolute ethanol, 8 mL of TMOS, 8 mL of ITMS, and 4 mL H_2O in a round-bottom flask (molar ratio: ITMS/TMOS/EtOH/ H_2O = 1:1.3:3.3:5.4). This mixture was maintained 1 day under stirring at RT (~ 22 °C). Afterward, 2 mL of a 5×10^{-4} M solution of **2** in EtOH was added to 3 mL of the sol solution, and the mixture was maintained under stirring at 50 °C for 1 h. The obtained sol was then dropcasted on a glass support and let dry at RT.

Analytical Data and Spectroscopic Characterization. Elemental Analysis. C, H, N analyses were performed with a Flash 2000 Fisher Scientific Thermo Electron Analyzer. Electronic UV-vis-NIR: DR on Teflon films and solution absorption spectra were collected using an Agilent Cary 5000 spectrophotometer. Vibrational spectroscopy: FT-IR spectra on KBr pellets were collected using a Bruker Equinox 55 spectrophotometer. ICP-mass determinations: 220 mg of a DMSO solution (5×10^{-4} M, approx) of the selected sample was introduced in a TFM vessel containing a mixture of HNO_3 (65%, 4 mL), H_2O_2 (30%, 0.5 mL), and H_2O (bidistilled, 4 mL) thus treated in a Milestone Ethos 1 Microwave digester, equipped with a HPR1000/10S high pressure segmented rotor, ATC-400CE automatic temperature control, and Terminal 640 with easyCONTROL software. The treatment was performed by applying a microwave program consisting of two steps each lasting 10 min at the temperature of 200 °C and microwave power up to 1000 W. The samples were prepared for the analysis by diluting the digested solutions with 5% HNO_3 (suprapur grade) blank, and then the metals were determined using a quadrupole ICP-mass Varian mod. RT equipped with a 90° reflecting ion mirror (Varian, Mulgrave, Australia), a Micromist glass low flow concentric nebulizer, a Peltier-cooled (3 °C) double pass glass spray chamber, and a glass torch, with respect to four-points external aqueous calibration plots in the 0.1–25 $\mu\text{g L}^{-1}$ range for each metal (correlation coefficients > 0.999990, limit of detection (LoD) for the different analytes: 0.5–5 ng L^{-1}). Instrumental parameters and measured isotopes are listed in Table S1 in the Supporting Information. ESI-mass: Mass spectra were obtained with a Micromass ZMD spectrometer operating in positive ionization mode. SEM-EDX. SEM-EDX analyses were performed with a FEI Dual Beam Nova NanoLab 600i equipped with a EDAX Genesis microanalyzer.

Structural and Crystallographic Studies. X-ray Powder Diffraction. Wide-angle XRD patterns on microcrystalline powder samples were recorded with a Panalytical Empyrean diffractometer equipped with a graphite monochromator and a X'Celerator linear detector. The scans were collected within the range 5–40° (2θ) using $\text{Cu K}\alpha$ radiation.

Data Collection and Structure Determination for 1b. A clear colorless needle-like specimen of **1b** of approximate dimensions 0.011 \times 0.019 \times 0.099 mm^3 was used for the X-ray crystallographic analysis. The X-ray intensity data were measured on a Bruker D8 VENTURE system equipped with a multilayer monochromator and a Mo $\text{K}\alpha$ Incoatec microfocus sealed tube ($\lambda = 0.71073$ Å). This instrumental setup was well suited for the collection of the small crystal sample. A total of 777 frames were collected, which were integrated with the Bruker SAINT software package using a narrow-frame algorithm.³² The integration of the data using a triclinic unit cell yielded a total of 40882 reflections to a maximum θ angle of 25.03° (0.84 Å resolution), Table 1. Data were corrected for absorption effects using the multiscan

method (SADABS V2012/1).^{33,34} The calculated minimum and maximum transmission coefficients (based on crystal size) were 0.660 and 0.951. The structure was solved and refined using XS and XL included in the APEX2 software suite^{35,36} using the space group P-1. The largest peak and hole in the final difference electron density synthesis were $2.484 \text{ e}^-/\text{\AA}^3$ and $-1.253 \text{ e}^-/\text{\AA}^3$, respectively. CCDC 1054887 contains the supplementary crystallographic data.

Photophysical Studies. Absorption and PL studies, except for doped thin films and crystalline samples, were performed on diluted ($5 \times 10^{-4} \text{ M}$) solutions of the strongly coordinating DMSO solvent to ensure that the observed properties are related to isolated molecules rather than to aggregates or clusters. CW visible PL spectra were recorded using a Horiba Jobin-Yvon FluoroMax-4 spectrofluorimeter. Transient PL was excited at 392 nm wavelength by the frequency-doubled, 130-fs-long output pulses of a regenerative Ti/Sapphire amplifier (Quantronix INTEGRA C) running at repetition frequency of 1 kHz. For silica thin films, PL in the NIR region was excited at 355 nm wavelength using the 310-ps-long output pulses of a passively Q-switched powerchip laser running at repetition frequency of 1 kHz. Visible PL decay transients were captured by a streak camera (Hamamatsu C5680) equipped with a grating spectrometer (Acton SpectraPro 2300i). NIR PL was wavelength dispersed by an Acton SpectraPro 2300i spectrometer; optical spectra and decay transients were detected using, respectively, an InGaAs CCD (Andor iDus) and a photomultiplier (Hamamatsu H10330A-75) connected to a 1 GHz digitizing oscilloscope (Tektronik TDS 5104). To minimize nonlinear effects possibly taking place in doubly excited complexes, photo-excitation fluences were kept below the level of 0.1 excitations per complex per laser pulse in all experiments. Transient photoinduced absorption was measured by broadband synchronous pulses obtained by supercontinuum generation in a sapphire plate. The optical probe beam transmitted through the sample was spectrally dispersed using a SpectraPro 2300i spectrograph and detected by a charge-coupled device (Andor NEWTON). Pump-probe time delay was varied using a motorized optical delay stage. Photoinduced absorption is measured as the differential transmission signal $\Delta T/T = (T - T_0)/T_0$, where T (T_0) is the transmitted probe pulse energy in presence (absence) of the pump pulse(s). PL measurements on crystalline samples were performed with an Edinburgh Instruments FLSP920 spectrofluorimeter equipped with a photomultiplier detector (Hamamatsu R5509-72 NIR PMT) and using a 450W xenon lamp as the steady state excitation source for NIR spectra and a Continuum Surelite I-10 Nd:YAG laser system (10 Hz repetition rate) using the third harmonic $\lambda_{\text{exc}} = 355 \text{ nm}$ for time-resolved dynamics.

■ ASSOCIATED CONTENT

Supporting Information

ICP-mass setup details; powder XRD patterns; EDX analysis; supplementary ESI-MS, spectroscopic, and PL data; details of kinetic equations; and curve fitting procedures. The Supporting Information is available free of charge on the ACS Publications website at DOI: 10.1021/acs.chemmater.5b01109.

■ AUTHOR INFORMATION

Corresponding Authors

*E-mail: f.artizzu@unica.it.

*E-mail: francesco.quochi@dsf.unica.it.

*E-mail: deplano@unica.it.

Notes

The authors declare no competing financial interest.

■ ACKNOWLEDGMENTS

The Regione Autonoma della Sardegna (CRP-17571) and Banco di Sardegna Foundation are gratefully acknowledged for financial support. The authors thank Dr. A. Rigoldi for ICP-mass and Drs. S. Podda and E. Musu (Laboratorio di Telemicroscopia Industriale, Sardegna Ricerche) for SEM-

EDX analyses. The authors thank Dr. Holger Ott of Bruker AXS (Karlsruhe) for the single crystal data collection. R.V.D. thanks the Flemish Hercules Foundation (Project No. AUGÉ/09/024 "Advanced Luminescence Setup") for funding.

■ REFERENCES

- Bünzli, J.-C. G.; Piguet, C. Taking Advantage of Luminescent Lanthanide Ions. *Chem. Soc. Rev.* **2005**, *34*, 1048–1077.
- Eliseeva, S. V.; Bünzli, J.-C. G. Lanthanide Luminescence for Functional Materials and Biosciences. *Chem. Soc. Rev.* **2010**, *39*, 189–227.
- Strohhofer, C.; Polman, A. Absorption and Emission Spectroscopy in Er^{3+} - Yb^{3+} Doped Aluminum Oxide Waveguides. *Opt. Mater.* **2003**, *21*, 705–712.
- Chryssou, C. E.; Di Pasquale, F.; Pitt, C. W. Improved Gain Performance in Yb^{3+} -Sensitized Er^{3+} -Doped Alumina (Al_2O_3) Channel Optical Waveguide Amplifiers. *J. Lightwave Technol.* **2001**, *19*, 345–349.
- Chiasera, A.; Tosello, C.; Moser, E.; Montagna, M.; Belli, R.; Goncalves, R. R.; Righini, G. C.; Pelli, S.; Chiappini, A.; Zampedri, L.; Ferrari, M. $\text{Er}^{3+}/\text{Yb}^{3+}$ -Activated Silica-Titania Planar Waveguides for EDPWAs Fabricated by RF-Sputtering. *J. Non-Cryst. Solids* **2003**, *322*, 289–294.
- Wong, W. H.; Pun, E. Y. B.; Chan, K. S. Er^{3+} - Yb^{3+} Codoped Polymeric Optical Waveguide Amplifiers. *Appl. Phys. Lett.* **2004**, *84*, 176–178.
- da Vila, L. D.; Gomes, L.; Tarelho, L. V. G.; Ribeiro, S. J. L.; Messadeq, Y. Mechanism of the Yb-Er Energy Transfer in Fluorozirconate Glass. *J. Appl. Phys.* **2003**, *93*, 3873–3880.
- Dong, B.; Feng, Z. Q.; Cao, B. S.; Zheng, J. Z. $\text{Yb}^{3+} \rightarrow \text{Er}^{3+}$ Energy Transfer in Al_2O_3 and Temperature Characteristic of Near-Infrared Photoluminescence. *J. Sol-Gel Sci. Technol.* **2009**, *50*, 383–386.
- Artizzu, F.; Quochi, F.; Marchiò, L.; Sessini, E.; Saba, M.; Serpe, A.; Mura, A.; Mercuri, M. L.; Bongiovanni, G.; Deplano, P. Fully Efficient Direct Yb-to-Er Energy Transfer at Molecular Level in a Near-Infrared Emitting Heterometallic Trinuclear Quinolinolate Complex. *J. Phys. Chem. Lett.* **2013**, *4*, 3062–3066.
- Artizzu, F.; Quochi, F.; Marchiò, L.; Fonseca Correia, R.; Saba, M.; Serpe, A.; Mura, A.; Mercuri, M. L.; Bongiovanni, G.; Deplano, P. Ln_3Q_9 as a Molecular Framework for Ion-Size-Driven Assembly of Heterolanthanide (Nd, Er, Yb) Multiple Near-Infrared Emitters. *Chem.—Eur. J.* **2015**, *21*, 3882–3885.
- Van Deun, R.; Fias, P.; Nockemann, P.; Schepers, A.; Parac-Vogt, T. N.; Van Hecke, K.; Van Meervelt, L.; Binnemans, K. Rare-Earth Quinolinates: Infrared-Emitting Molecular Materials with a Rich Structural Chemistry. *Inorg. Chem.* **2004**, *43*, 8461–8469.
- Artizzu, F.; Deplano, P.; Marchiò, L.; Mercuri, M. L.; Pilia, L.; Serpe, A.; Quochi, F.; Orrù, R.; Cordella, F.; Meinardi, F.; Tubino, R.; Mura, A.; Bongiovanni, G. Structure and Emission Properties of Er_3Q_9 ($\text{Q} = 8$ -Quinolinolate). *Inorg. Chem.* **2005**, *44*, 840–842.
- Leary, S. G.; Deacon, G. B.; Junk, P. C. The Synthesis of a Homoleptic Lanthanoid Complex of the 8-Quinolinolate Ion Directly from the Metal. *Z. Anorg. Allg. Chem.* **2005**, *631*, 2647–2650.
- Baranov, E. V.; Fukin, G. K.; Balashova, T. V.; Pushkarev, A. P.; Grishin, I. D.; Bochkarev, M. N. 8-Quinolinolate Complexes of Yttrium and Ytterbium: Molecular Arrangement and Fragmentation Underlaser Impact. *Dalton Trans.* **2013**, *42*, 15699–15705.
- Chilton, N. F.; Deacon, G. B.; Gazukin, O.; Junk, P. C.; Kersting, B.; Langley, S. K.; Moubaraki, B.; Murray, K. S.; Schleife, F.; Shome, M.; Turner, D. R.; Walker, J. A. Structure, Magnetic Behavior, and Anisotropy of Homoleptic Trinuclear Lanthanoid 8-Quinolinolate Complexes. *Inorg. Chem.* **2014**, *53*, 2528–2534.
- Quochi, F.; Saba, M.; Artizzu, F.; Mercuri, M. L.; Deplano, P.; Mura, A.; Bongiovanni, G. Ultrafast Dynamics of Intersystem Crossing and Resonance Energy Transfer in $\text{Er}(\text{III})$ -Quinolinolate Complexes. *J. Phys. Chem. Lett.* **2010**, *1*, 2733–2737.

(17) Artizzu, F.; Quochi, F.; Saba, M.; Marchiò, L.; Espa, D.; Serpe, A.; Mura, A.; Mercuri, M. L.; Bongiovanni, G.; Deplano, P. Dual Emitting $[\text{Yb}(\text{S},7\text{ClQ})_2(\text{HS},7\text{ClQ})_2\text{Cl}]$: Chemical and Photophysical Properties. *ChemPlusChem* **2012**, *77*, 240–248.

(18) Curry, R. J.; Gillin, W. P. 1.54 μm Electroluminescence from Erbium(III) Tris(8-hydroxyquinoline) (ErQ)-Based Organic Light-Emitting Diodes. *Appl. Phys. Lett.* **1999**, *75*, 1380–1382.

(19) Khreis, O. M.; Gillin, W. P.; Somerton, M.; Curry, R. J. 980 nm Electroluminescence from Ytterbium Tris(8-hydroxyquinoline). *Org. Electron.* **2001**, *2*, 45–51.

(20) Penna, S.; Reale, A.; Pizzoferrato, R.; Tosi Belleffi, G. M.; Musella, D.; Gillin, W. P. Near-Infrared Photoluminescence of Erbium Tris(8-hydroxyquinoline) Spin-Coated Thin Films Induced by Low Coherence Light Sources. *Appl. Phys. Lett.* **2007**, *91*, 021106.

(21) Figus, C.; Quochi, F.; Artizzu, F.; Piana, G.; Saba, M.; Mercuri, M. L.; Serpe, A.; Deplano, P.; Mura, A.; Bongiovanni, G. Sol-Gel Silica Films Embedding NIR-Emitting Yb–Quinolinolate Complexes. *AIP Conf. Proc.* **2014**, *1624*, 37–42.

(22) Artizzu, F.; Quochi, F.; Saba, M.; Loche, D.; Serpe, A.; Mercuri, M. L.; Mura, A.; Bongiovanni, G.; Deplano, P. Silica Sol-Gel Glasses Incorporating Dual-Luminescent Yb–Quinolinolate Complex: Processing, Emission, and Photosensitising Properties of the “Antenna” Ligand. *Dalton Trans.* **2012**, *41*, 13147–13153.

(23) Binnemans, K. Lanthanide-Based Luminescent Hybrid Materials. *Chem. Rev.* **2009**, *109*, 4283–4374.

(24) Armelao, L.; Quici, S.; Barigelletti, F.; Accorsi, G.; Bottaro, G.; Cavazzini, M.; Tondello, E. Design of Luminescent Lanthanide Complexes: From Molecules to Highly Efficient Photo-Emitting Materials. *Coord. Chem. Rev.* **2010**, *254*, 487–505.

(25) O’Riordan, A.; Van Deun, R.; Mairiaux, E.; Moynihan, S.; Fias, P.; Nockemann, P.; Binnemans, K.; Redmond, G. Synthesis of a Neodymium–Quinolate Complex for Near-Infrared Electroluminescence Applications. *Thin Solid Films* **2008**, *516*, 5098–5102.

(26) Artizzu, F.; Quochi, F.; Serpe, A.; Sessini, E.; Deplano, P. Tailoring Functionality through Synthetic Strategy in Heterolanthanide Assemblies. *Inorg. Chem. Front.* **2015**, *2*, 213–222.

(27) Bünzli, J.-C. G.; Piguët, C. Lanthanide-Containing Molecular and Supramolecular Polymetallic Assemblies. *Chem. Rev.* **2002**, *102*, 1897–1928.

(28) Ballardini, R.; Varani, G.; Indelli, M. T.; Scandola, F. Phosphorescent 8-Quinolinol Metal Chelates. Excited-State Properties and Redox Behavior. *Inorg. Chem.* **1986**, *25*, 3858–3865.

(29) Bischof, C.; Wahsner, J.; Scholten, J.; Trosien, S.; Seitz, M. Quantification of C-H Quenching in Near-IR Luminescent Ytterbium and Neodymium Cryptates. *J. Am. Chem. Soc.* **2010**, *132*, 14334–14335.

(30) Monguzzi, A.; Milani, A.; Mech, A.; Brambilla, L.; Tubino, R.; Castellano, C.; Demartin, F.; Meinardi, F.; Castiglioni, C. Predictive Modeling of the Vibrational Quenching in Emitting Lanthanides Complexes. *Synth. Met.* **2012**, *161*, 2693–2699.

(31) Quochi, F.; Orrù, R.; Cordella, F.; Mura, A.; Bongiovanni, G.; Artizzu, F.; Deplano, P.; Mercuri, M. L.; Pilia, L.; Serpe, A. Near-Infrared Light Emission Quenching in Organolanthanide Complexes. *J. Appl. Phys.* **2006**, *99*, 053520.

(32) S_AI_NT V8.34A; Bruker AXS Inc.: Madison, WI, 2007.

(33) S_AD_AB_S V2012/1; Bruker AXS Inc.: Madison, WI, 2001.

(34) Krause, L.; Herbst-Irmer, R.; Sheldrick, G. M.; Stalke, D. Comparison of Silver and Molybdenum Microfocus X-ray Sources for Single-Crystal Structure Determination. *J. Appl. Crystallogr.* **2015**, *48*, 3–10.

(35) Sheldrick, G. M. A Short History of SHELXL. *Acta Crystallogr., Sect. A: Found. Crystallogr.* **2008**, *64*, 112–122.

(36) Sheldrick, G. M. Crystal Structure Refinement with SHELXL. *Acta Crystallogr., Sect. C: Struct. Chem.* **2015**, *71*, 3–8.